INORGANIC CHEMISTRY FRONTIERS

RESEARCH ARTICLE

View Article Online
View Journal | View Issue

Cite this: *Inorg. Chem. Front.*, 2022, **9**, 3728

Modulated luminescence of zero-dimensional bimetallic all-inorganic halide clusters†

Chao Zhang,‡[a] Xuezhen Feng,‡[b] Qilin Song,[a] Chaocheng Zhou,[a] Lin Peng,[a] Xiaolin Liu,*[a] Hong Chen *[b] and Jia Lin *[a]

Received 23rd March 2022,
Accepted 11th June 2022

DOI: 10.1039/d2qi00620k

rsc.li/frontiers-inorganic

Zero-dimensional (0D) metal halide clusters formed as isolated metal halide polyhedral structures show excellent optical properties and have great potential for various applications in optoelectronic devices. In this study, we reported a series of $Rb_8CuB(III)_3Cl_{18}$ single crystals (SCs) constructed from Cu(I) and B(III) (B = In, Tb, *etc.*) containing lead-free bimetallic halide clusters. Density functional theory calculations have been used to explore the thermodynamic stability of the expected bimetallic halide clusters, in which the ionic radius of B(III) trivalent metal cations should be within the range of 0.74 to 0.99 Å in order to form a stable $Rb_8CuB(III)_3Cl_{18}$ 0D structure in line with the same structure configuration. By analyzing the effects of different B(III) cations on the structural parameters and optical-physical properties, we found that the luminescence of SCs could be modulated by different B(III) cations, while the luminescence originated from the charge transfer from Cu(I) ions to metal-chloride octahedra. This study reported the rational design of novel-structured Cu(I)-based inorganic lead-free metal halide materials, which paves the way for the exploration of new luminescent materials.

Introduction

Halide perovskites, with a chemical formula of ABX_3 (where A represents Cs^+, MA^+ or FA^+, *etc.*; B represents Pb^{2+} or Sn^{2+}, *etc.*; and X represents halide ions), have attracted significant attention attributed to their excellent optoelectronic properties, such as high light absorption coefficient, long carrier diffusion length, and tunable bandgap.[1–4] Such outstanding properties make them potential candidates for solar cells,[5–8] light-emitting diodes,[9–12] and detectors.[13–16] Currently, large-scale applications of halide perovskites are plagued by the toxicity of lead (Pb^{2+}).[17] Replacing Pb^{2+} with other nontoxic elements while maintaining excellent properties has become a challenge. Lead-free luminescent perovskite materials are of great emergency. In previous reports, Pb^{2+} has been replaced with divalent Sn^{2+} or Ge^{2+}, and trivalent Bi^{3+} or Sb^{3+}, because these cations have an identical electron configuration to Pb^{2+}, but less toxicity. However, the divalent Sn^{2+} or Ge^{2+} in the perovskite structure can be easily oxidized to tetravalent Sn^{4+} or Ge^{4+}, which affects the framework stability and optical performance of the perovskite structure.[18–20] Simply employing +3 valence state cations to construct a single B site perovskite limits the possibility of forming a three-dimensional (3D) corner-shared perovskite structure due to the charge balance problem. Low-dimensional crystal structures, such as $A_2B(III)X_5$, $A_3B(III)X_6$, and $A_3B(III)_2X_9$, are frequently achieved. Such perovskite-related metal halides usually have larger optical bandgaps and lower carrier mobilities than 3D perovskites, which are unsuitable for photovoltaic devices. Moreover, by replacing two Pb^{2+} ions with a +1 and +3 cation pair, double perovskite structure $A_2B(I)B(III)X_6$ can be formed, in which two kinds of octahedra arrange alternately. However, due to the strong local electric field between the ordered B(I) and B(III) sites in the 3D lattice, the double perovskites show inferior optoelectronic performance than conventional 3D perovskites.[21,22]

To tune the luminescence properties of perovskites, the dimensional engineering of halide materials has been heavily employed. By limiting the coordination number of metal ions at the B(I) position in double perovskites, the low coordination prevents the B(I) metal atoms from forming octahedra with the surrounding halogens. This integration disintegrates the 3D double perovskite structure, leading to the formation of lower-dimensional structures. As a result, the electrical conductivity

[a]*Department of Physics, Shanghai University of Electric Power, Shanghai 200090, China. E-mail: xlliu@shiep.edu.cn, jlin@shiep.edu.cn*
[b]*Shenzhen Key Laboratory of Interfacial Science and Engineering of Materials, State Environmental Protection Key Laboratory of Integrated Surface Water-Groundwater Pollution Control, Guangdong Provincial Key Laboratory of Soil and Groundwater Pollution Control, School of Environmental Science and Engineering, Southern University of Science and Technology, Shenzhen 518055, China. E-mail: chenh3@sustech.edu.cn*

†Electronic supplementary information (ESI) available. CCDC 2128946 ($Rb_8CuIn_3Cl_{18}$) and 2128947 ($Rb_8CuTb_3Cl_{18}$). For ESI and crystallographic data in CIF or other electronic format see DOI: https://doi.org/10.1039/d2qi00620k

‡These authors contributed equally to this work.

toward the metal halide bond network is reduced.[23,24] The low-dimensional metal halides possess high exciton binding energies and large bandgaps due to quantum and dielectric limitations.[25,26] In addition, increasingly isolated octahedral units would enhance exciton localization, which in turn enhances radiative recombination, resulting in high luminescence efficiencies.[27–29]

In this study, based on the idea of replacing Pb(II) ions with monovalent Cu(I) ions and trivalent In(III) ions, we introduced a new all-inorganic copper–indium halide structure, $Rb_8CuIn_3Cl_{18}$. The single crystals (SCs) were synthesized *via* a vacuum solid-state reaction method, preventing the influence of water and oxygen during the SC growing process. The Cu(I) ion has been chosen because the Cu $3d^{10}$ electron is unstable at its high energy level and must be hybridized with 4*s* and 4*p* states to reduce the energy. Lower coordination numbers of Cu(I) with halides distorted the d^{10} orbitals, resulting in stronger *d*–*s* and *d*–*p* hybridization, thus, debarring the formation of 6-fold coordination.[30] Considering the thermodynamic stability and octahedral factors, we further constructed a series of zero-dimensional (0D) clusters based on this crystal structure and investigated the relationship between the structural stability and radius of trivalent-metal cations. We concluded that stable Cu-based cluster structures could be formed only when the ionic radius of trivalent-metal cations was within 0.74–0.99 Å, and the optimum structure appeared to have an ionic radius of 0.86 Å. Combining the optical properties with structural data of the reported isomorphic SCs, we further elucidated the luminescence mechanism in the obtained materials.

Results and discussion

The novel luminescent all-inorganic lead-free metal halide $Rb_8CuIn_3Cl_{18}$ SCs were obtained *via* a vacuum solid-phase reaction method.[31] From the pre-synthesis experiments, we found that the growth temperature of $Rb_8CuIn_3Cl_{18}$ SCs was lower than the average melting point of all the involved precursors. Thus, the target product cannot be obtained *via* a one-pot solid-chemistry synthesis. Under this circumstance, the entire SC growth process needs to be divided into two steps: pre-crystallization and re-crystallization. As displayed in Fig. 1a, RbCl, CuCl, and $InCl_3$, with the mole ratio of 8 : 1 : 3, were ground and sealed in a 9 mm-diameter quartz ampoule in a vacuum. The as-prepared quartz ampoule was annealed in a muffle furnace at 700 °C for 24 h and then cooled to room temperature. The main product obtained at the high temperature was confirmed to be Rb_3InCl_6 using powder X-ray diffraction (PXRD) (Fig. S1†). After that, the quartz ampoule contain-

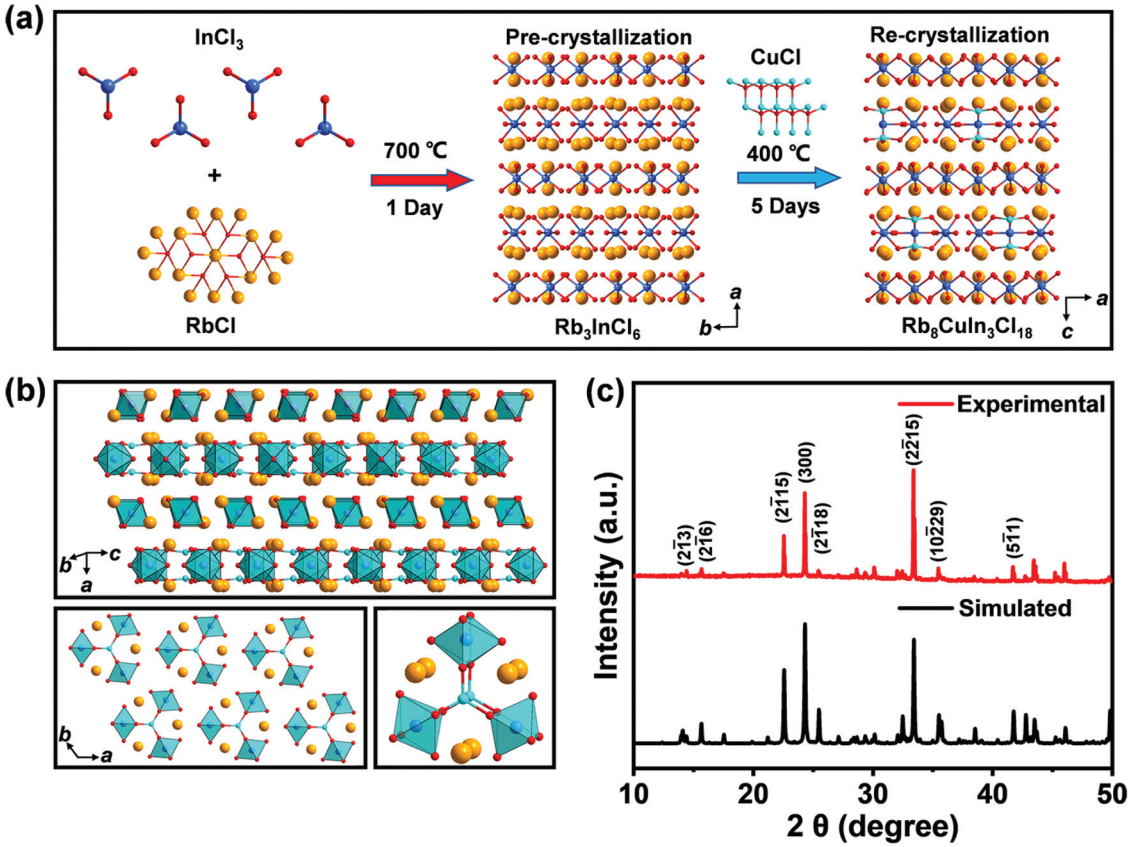

Fig. 1 (a) Schematic of the preparation process of $Rb_8CuIn_3Cl_{18}$ SCs. (b) View of structural characteristics of $Rb_8CuIn_3Cl_{18}$ SCs. Color scheme: orange, Rb atoms; light blue, Cu atoms; dark blue, In atoms; red, Cl atoms. (c) Experimental and simulated PXRD patterns.

ing Rb_3InCl_6 SCs was annealed at 400 °C for 5 days. The block-like $Rb_8CuIn_3Cl_{18}$ SCs were obtained after cooling to room temperature.

To understand the two-step growth process of $Rb_8CuIn_3Cl_{18}$ SCs, thermal stability was analyzed using thermogravimetry-differential scanning calorimetry (TG-DSC) under a nitrogen atmosphere. The white sample powder was heated from 25 to 800 °C at a constant rate of 10 °C min^{-1}. No weight loss was found until the temperature increased to 400 °C (Fig. S2†). The thermal stability was slightly lower than the previously reported low-dimensional all-inorganic Cu(I)-based halides such as Rb_2CuCl_3, $CsCu_2Cl_3$, and $Cs_3Cu_2Cl_5$.[32–34] This may be related to the nature of the 3-fold coordination number of Cu(I) in $Rb_8CuIn_3Cl_{18}$. When the temperature increased from 400 to 650 °C, the sample powder lost 15.54% of the weight. From the TG-DSC curves, the thermal decomposition process of $Rb_8CuIn_3Cl_{18}$ SCs above 650 °C is consistent with that of Rb_3InCl_6 SCs, indicating that the weight lost can be ascribed to the destruction of the Cu–Cl bond in $Rb_8CuIn_3Cl_{18}$ and the formation of Rb_3InCl_6 (Fig. S2†). After raising the temperature above 650 °C, the sample powder continued to lose weight, indicating the thermal decomposition of Rb_3InCl_6. The different formation energies of Rb_3InCl_6 and $Rb_8CuIn_3Cl_{18}$ structures could further shed light on the necessity of multi-step preparation. The formation energy of $Rb_8CuIn_3Cl_{18}$ (−5.34 eV) is much lower than that of Rb_3InCl_6 (−1.0 eV), which means that in order to avoid Rb_3InCl_6 impurities, the growth of $Rb_8CuIn_3Cl_{18}$ SCs needs a lower temperature environment. Therefore, 700 °C and 400 °C were selected as the pre-crystallization and re-crystallization temperatures to prepare $Rb_8CuIn_3Cl_{18}$ SCs, respectively.

The crystal structure of the novel $Rb_8CuIn_3Cl_{18}$ SCs was determined by single-crystal X-ray diffraction (SCXRD). $Rb_8CuIn_3Cl_{18}$ SCs displayed a monoclinic structure with a space group of $R3c$ ($Z = 3$, $a = b = 12.656$ Å, $c = 75.15$ Å). The detailed crystallographic data and experimental refinement parameters are shown in Table S1,† and the bond lengths are listed in Table S2.† The asymmetric unit in the crystal structure of $Rb_8CuIn_3Cl_{18}$ consisted of two types of layers (Fig. 1b). Type I layer consisted of spatially well-isolated $[InCl_6]^{3-}$ octahedra with surrounding Rb^+ cations, similar to that in Rb_3InCl_6 SCs (Fig. S3†).[29] Each $[InCl_6]^{3-}$ octahedron was composed of a unique In site in a 3+ oxidation state coordinated by six chlorine anions, with an average In–Cl bond length of 2.505 Å. In the type II layer, two Cu(I) ions combined with three $[InCl_6]^{3-}$ octahedra to form a paddle-wheel-like $[Cu_2(InCl_6)_3]^{7-}$ cluster, and the clusters were separated by Rb^+. The average In–Cl bond length in the cluster was 2.525 Å, which was almost equal to that in the type I layer. The two types of layers stacked alternatively along the c-axis following the 6_1 screw axis symmetry, forming a trigonal structure. The PXRD pattern of the as-synthesized $Rb_8CuIn_3Cl_{18}$ powder matched well with the simulated one obtained from SCXRD (Fig. 1c), certifying the purity of $Rb_8CuIn_3Cl_{18}$ SCs. Energy-dispersive X-ray spectroscopy (EDS) mapping showed a uniform distribution of Rb, Cu, In, and Cl elements (Fig. S4†), in which the atomic ratio of Rb/Cu/In/Cl was determined to be 7.86 : 1 : 3.06 : 17.15, which was approximately equal to the stoichiometric proportion of the structure formula as obtained from SCXRD.

In our previous work, $Rb_8B(I)Sc_3Cl_{18}$ SCs were synthesized by using d^{10} monovalent metal-cationic Cu(I) or Ag(I) occupying the B(I)-site, respectively.[22] By analyzing their luminescence properties, it was considered that the metal cation at the B(I)-site was the switch of the luminescence of the 0D structure because the B(I) ion oxidation characteristics in the cluster determined whether the SCs were emissive. Here, we further explored the influence of B(III) ions on the overall structure by considering the thermodynamic stability and structural factors. A series of $Rb_8CuB(III)_3Cl_{18}$ structural models were constructed by using different B(III) ions. The Cu–Cl bond lengths in these optimized structural models are shown in Fig. 2a. When the trivalent-metal cation radius was between 0.67 and 0.99 Å, the Cu–Cl bond length was less than 2.6 Å, which was within the typical Cu–Cl bond length range (Table S3†). If the

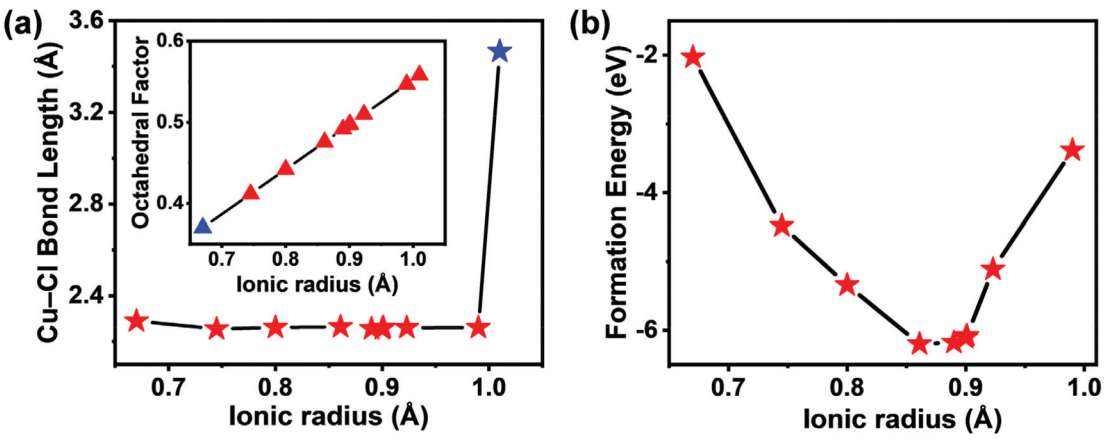

Fig. 2 (a) Relationship between the radius of B(III) ions and Cu–Cl bond lengths of $Rb_8CuB(III)_3Cl_{18}$ SCs. Inset: Octahedral factors of $Rb_8CuB(III)_3Cl_{18}$ compounds. The red triangle shows that the structure can form at room temperature under ambient pressure, whereas the blue triangle indicates that the structure is unstable. (b) The formation energy of $Rb_8CuB(III)_3Cl_{18}$ SCs with different B(III) ionic radius.

B(III) ion had a radius of 1.01 Å, the distance between Cu ion and the nearest Cl ion was 3.47 Å, which was much larger than the maximum value of the Cu–Cl bond. In addition, the octahedral factor is an important criterion to predict the stability of the perovskite structure,[35,36] described by the formula $\mu = r_B/r_X$ (where r_B represents the ionic radius of B(III) cations, and r_X represents the ionic radius of halogen). When r_B was less than 0.74 Å, μ was less than 0.41, and the lattice tended to be distorted to form a layered geometry with edge- or face-sharing polyhedra, thus, failing to form stable cluster structures. As shown in Fig. 2b, the formation energy of structures with different B(III) cations first decreased and then increased with increasing ionic radius. The ionic radius of 0.86 Å referred to the minimum formation energy of −6.2 eV, illustrating that the radius of B(III) cations should be within 0.74 and 0.99 Å to form this type of Cu(I)-connected octahedral clusters. We selected rare-earth ions to build the models because of two reasons. First, rare-earth ions show a stable trivalent state which satisfies the valence requirements. Second and more importantly, rare-earth elements have the same outermost structure of two s electrons, resulting in similar physical and chemical properties. The selection of rare-earth elements could effectively avoid the interference of chemical activity, electronegativity, melting point, and other factors for predicting the influence of the B(III) ionic radius on the structure. To verify the accuracy of the calculation results, we used the same solid-state method to synthesize a new 3-fold coordinated Cu(I)-based SCs with the same structure as $Rb_8CuIn_3Cl_{18}$, however, with different B(III) ionic radius, namely $Rb_8CuTb_3Cl_{18}$. As confirmed by SCXRD, $Rb_8CuTb_3Cl_{18}$ crystallized within the same space group of $R3c$. A paddle-wheel-like cluster structure has been involved in the crystal structure (Fig. S5†). The Cu–Cl bond lengths obtained from SCXRD were consistent with the calculated value (Table S4†).

In the following, the photophysical properties of $Rb_8CuIn_3Cl_{18}$ SCs were explored. From the UV-visible absorption spectrum (Fig. 3a), the $Rb_8CuIn_3Cl_{18}$ SCs had a distinct absorption edge at approximately 376 nm, with an estimated bandgap of 3.19 eV. The steady-state photoluminescence (PL) spectrum of $Rb_8CuIn_3Cl_{18}$ displayed a broadband emission with a peak centered at 482 nm (2.57 eV) under 305 nm excitation (Fig. 3b). The large Stokes shift of 177 nm suggested that the PL of $Rb_8CuIn_3Cl_{18}$ SCs was not from the band-edge emission. The PL quantum yield (PLQY) of $Rb_8CuIn_3Cl_{18}$ SCs

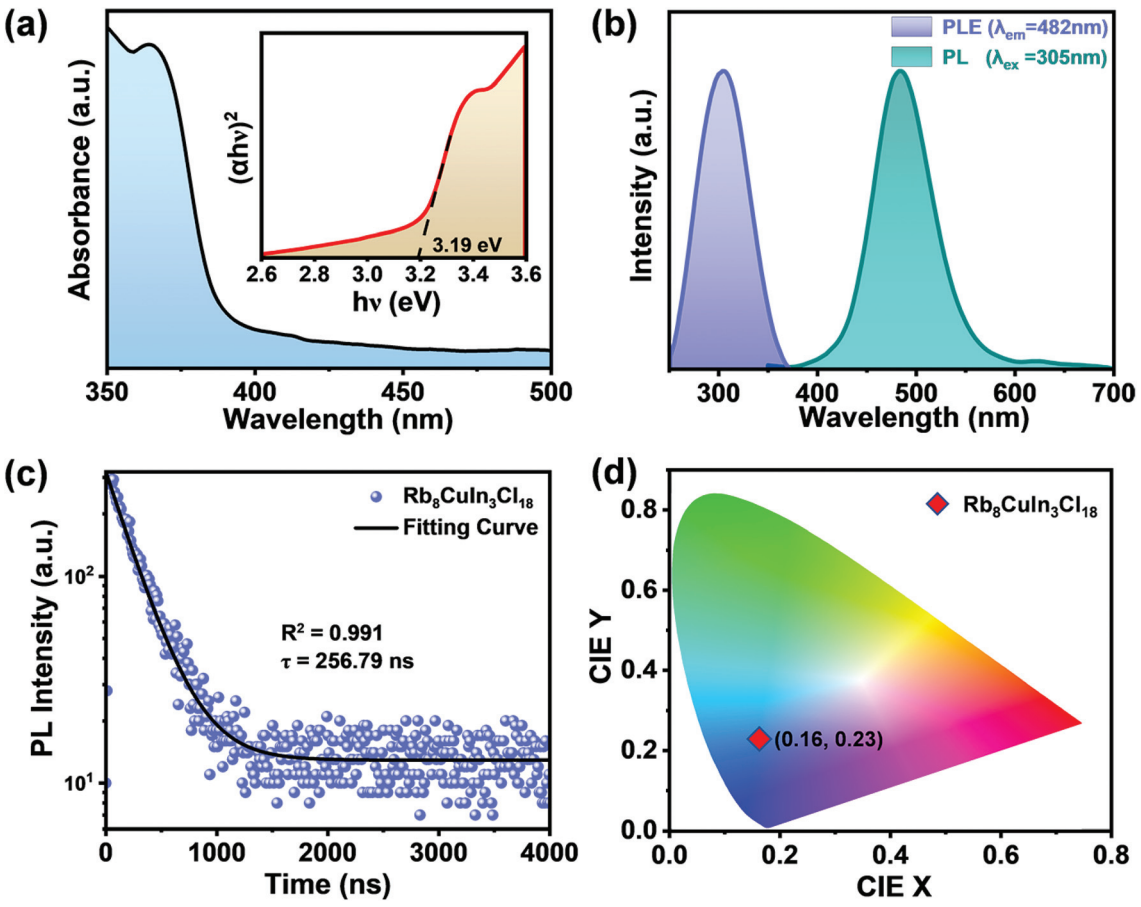

Fig. 3 (a) Absorption spectrum of $Rb_8CuIn_3Cl_{18}$ SCs. Inset: The corresponding Tauc plot. (b) Excitation (purple line) and emission (green line) spectra of $Rb_8CuIn_3Cl_{18}$ SCs. (c) Fitting of the PL decay curve. (d) Chromaticity CIE coordinate.

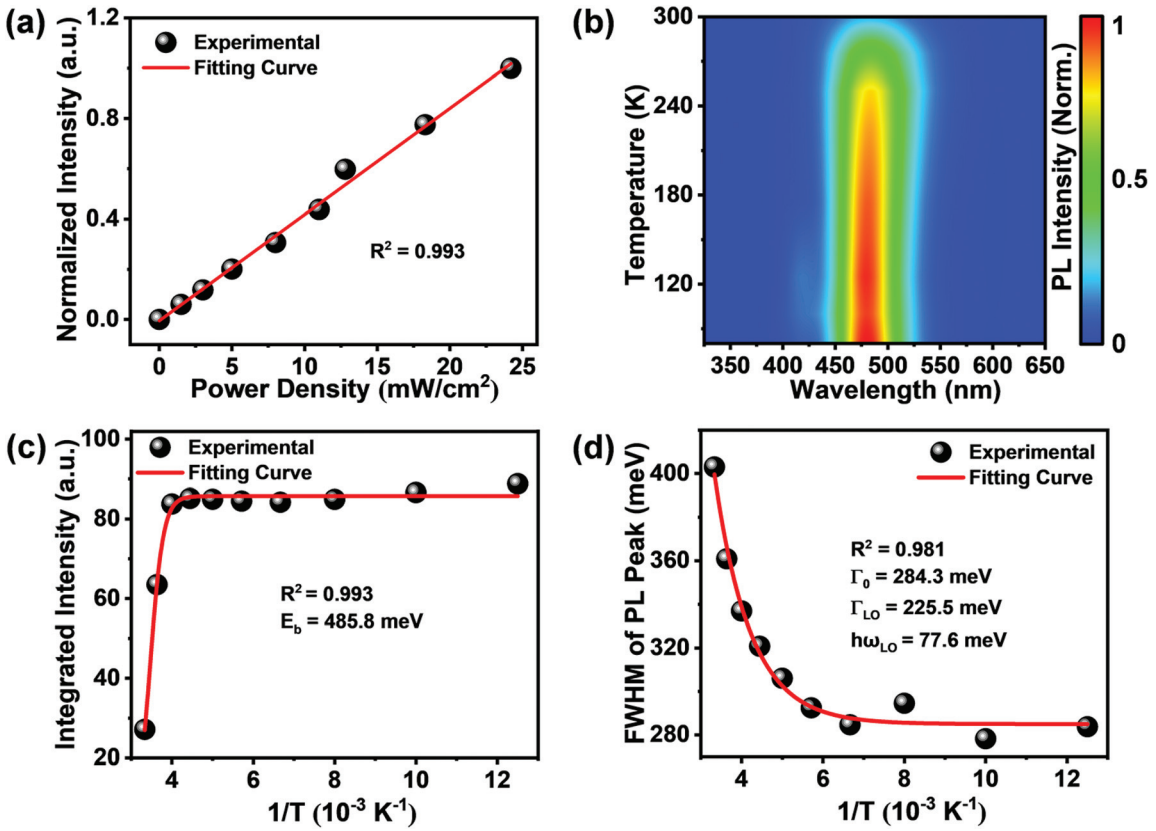

Fig. 4 (a) Power-dependent PL intensity of $Rb_8CuIn_3Cl_{18}$ SCs. (b) Temperature-dependent PL spectra under 305 nm excitation. (c, d) Variation of PL intensity and FWHM with temperature and the fitting curves.

was approximately 4%. Although the performance was not exceptional compared with other 0D metal halides, it performed better than all-inorganic 3D $CsPbX_3$ SCs with approximately 1% PLQY.[37] From the PL decay curve (Fig. 3c), a carrier lifetime of approximately 257 ns was determined. The CIE coordinate of $Rb_8CuIn_3Cl_{18}$ SCs was (0.16, 0.23) (Fig. 3d), corresponding to the sky-blue emission. For $Rb_8CuTb_3Cl_{18}$ SCs, the luminescence properties were consistent with the intrinsic luminescence of Tb^{3+} due to the transition between different energy levels of 4*f* electrons (Fig. S6†).[38,39] In addition, the material stability was evaluated. $Rb_8CuIn_3Cl_{18}$ SCs showed good stability under ambient conditions (25 °C, 50% ± 5% relative humidity), and significant emission was observed at 482 nm after 5 h of aging (Fig. S7†). In comparison, $Rb_8CuB(III)_3Cl_{18}$ SCs with rare-earth ions at the B(III) site decomposed very quickly and became non-emissive after exposure to air for a few minutes.

The variation of PL intensity with the excitation power density of $Rb_8CuIn_3Cl_{18}$ SCs was investigated. The PL intensity increased linearly with the excitation power density (Fig. 4a), suggesting that the emission was not from permanent defects.[40] The temperature-dependent PL spectra of $Rb_8CuIn_3Cl_{18}$ SCs in the temperature range of 80–300 K are shown in Fig. 4b. As the temperature decreased, the PL intensity increased. The variation of the integrated PL intensity with temperature can be fitted using an Arrhenius equation (Fig. 4c):[41]

$$I(T) = \frac{I_0}{1 + Ae^{E_b/(k_B T)}} \quad (1)$$

where $I(T)$ is the PL intensity at temperature T, I_0 is the value of PL intensity at temperature 0 K, E_b is the exciton binding energy, and k_B is the Boltzmann constant. The extracted exciton binding energy was 485.8 meV, which was much higher than that of the 3D $CsPbX_3$ perovskite (E_b values of approximately 2–55 meV), indicating that Frankel-type excitons dominated the emission process of $Rb_8CuIn_3Cl_{18}$ SCs.[42,43]

The exploration of temperature-dependent PL broadening helps in the understanding of the electron–phonon coupling mechanism. The full width at half-maximum (FWHM) of the PL peak declined with decreasing temperature (Fig. 4d), which can be fitted using the following formula:

$$\Gamma(T) = \Gamma_0 + \sigma T + \frac{\Gamma_{LO}}{e^{\hbar\omega_{LO}/k_B T} - 1} \quad (2)$$

where $\Gamma(T)$ and Γ_0 represent the FWHM at temperature T and 0 K, respectively; σ refers to the interaction between excitons and acoustic phonons, and is usually negligible; Γ_{LO} is the interaction between excitons and optical phonons; and $\hbar\omega_{LO}$ is the optical phonon energy. The values of Γ_0, Γ_{LO}, and $\hbar\omega_{LO}$

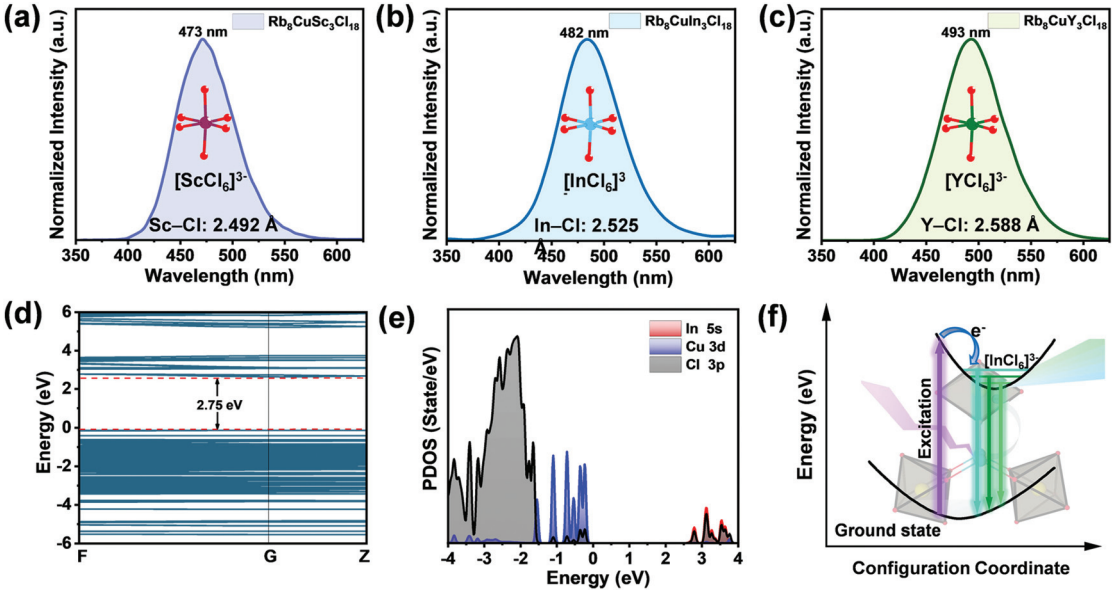

Fig. 5 Luminescence peak position and B(III)–Cl bond length in (a) $Rb_8CuSc_3Cl_{18}$, (b) $Rb_8CuIn_3Cl_{18}$, and (c) $Rb_8CuY_3Cl_{18}$. (d) Calculated electronic band structure and (e) PDOS of $Rb_8CuIn_3Cl_{18}$. (f) Schematic of the luminescence mechanism.

were 284.3, 225.5, and 77.6 meV, respectively. The exciton–phonon coupling strength was higher than that of the 3D hybrid perovskite (Γ_{LO} values of 40–61 meV),[44] whereas it was similar to that of double perovskites (approximately 230 meV).[45]

The luminescence mechanism of 0D metal halide $Rb_8Cu(I)B(III)_3Cl_{18}$ was further discussed. In our earlier work, under 375 nm light excitation, $Rb_8CuSc_3Cl_{18}$ and $Rb_8CuY_3Cl_{18}$ SCs showed strong and broad PL emissions. Rare-earth ions of Sc^{3+} and Y^{3+}, unlike Tb^{3+} and Eu^{3+}, had empty 4*f*-orbitals which did not exhibit emission caused by *f*–*f* transition. It was hypothesized that the luminescence of the SCs might come from the $[B(III)Cl_6]^{3-}$ octahedra. $Rb_8CuIn_3Cl_{18}$ SCs showed a single emission peak at 482 nm under 305 nm light excitation, in which In^{3+}, similar to Sc^{3+} and Y^{3+} ions, had no intrinsic luminescence properties. Therefore, we deduced that the luminescence of $Rb_8CuIn_3Cl_{18}$, similar to $Rb_8CuSc_3Cl_{18}$ and $Rb_8CuY_3Cl_{18}$, was relevant to the metal halide octahedra due to the unique isolated building units.[46,47]

To explore the effect of different B(III) ions on the luminescence properties of the $Rb_8Cu(I)B(III)_3Cl_{18}$ structure, we analyzed the relationship between the length of B(III)–Cl bond in the $[B(III)Cl_6]^{3-}$ octahedra and the emission peak position. As illustrated in Fig. 5a–c, the average B(III)–Cl (B = In, Sc, Y) bond lengths in the three compounds were 2.525 Å, 2.492 Å, and 2.588 Å, respectively. The In–Cl bond length was in between the Sc–Cl and Y–Cl bond lengths. Furthermore, the emission peak position of $Rb_8CuIn_3Cl_{18}$ was just located between that of $Rb_8CuSc_3Cl_{18}$ and $Rb_8CuY_3Cl_{18}$. The results indicated that the origins of luminescence of $Rb_8CuB(III)_3Cl_{18}$ (B(III) = In, Sc, Y) were consistent and related to the $[B(III)Cl_6]^{3-}$ octahedra. The emitting wavelength of this cluster structure could be tuned by selecting B(III) ions with different ionic radii, endowing this kind of material with a broader range of applications.[48]

$Rb_8CuIn_3Cl_{18}$ had a similar structure to Rb_3InCl_6. However, their optical properties were very different. Rb_3InCl_6 had an emission center at 436 nm, and its PL lifetime reached the microsecond level.[29,49,50] This indicated that Cu(I) ions in the cluster structure played a crucial role in the luminescence process of the SCs. Furthermore, we used density functional theory (DFT) calculations to explore the electron interactions in $Rb_8CuIn_3Cl_{18}$ and elucidate the role of Cu(I) in the luminescence process. The $[Cu_2(InCl_6)_3]^{7-}$ octahedral clusters in $Rb_8CuIn_3Cl_{18}$ were isolated by Rb^+ and their coupling was negligible, resulting in flat bands similar to other 0D structures (Fig. 5d).[51] From the projected density of states (PDOS) in Fig. 5e, the top of the valence band mainly consisted of the Cu *d* orbital, and the bottom of the conduction band was composed of In *s* and Cl *p* orbitals. This was consistent with the role of Cu(I) in $Rb_8CuSc_3Cl_{18}$ and $Rb_8CuY_3Cl_{18}$. Similar to the previously reported luminescence process of Cu(I)-based structures, the luminescence came from the intersystem crossing process.[52,53] Upon excitation, Cu(I) ions could be oxidized,[54] and the electrons were transferred to the connecting $[InCl_6]^{3-}$ octahedra in the cluster, making the octahedra the source of the broadband emission (Fig. 5f). To sum up, the luminescence properties of the $Rb_8CuB(III)_3Cl_{18}$ structure could be modulated by the Cu(I)-connected $[B(III)Cl_6]^{3-}$ octahedra. With the increase of the ionic radius of B(III), the $[B(III)Cl_6]^{3-}$ octahedra gradually expanded, accompanied by a continuous red shift of the luminescence.

Conclusion

This study has reported a series of novel all-inorganic Cu(I) based metal halide $Rb_8CuB(III)_3Cl_{18}$ (B = In, Tb, *etc.*) SCs. This

kind of structure was composed of alternating $[B(III)Cl_6]^{3-}$ octahedral and $[Cu_2(B(III)Cl_6)_3]^{7-}$ cluster layers. In each cluster, three $[B(III)Cl_6]^{3-}$ octahedra were connected to two Cu(I) ions to form a paddle-wheel cluster. By DFT calculations, we found that the paddle-wheel-like cluster structure could be created only when the ionic radius of B(III) trivalent metal cations was in the range of 0.74 to 0.99 Å. After studying the relationship between the structures and luminescence properties of $Rb_8CuB(III)_3Cl_{18}$ SCs with different B(III) ions, we found that all the luminescence of these SCs was determined by both B(I) connecting ions and B(III) ions in the octahedral centers. Furthermore, the luminescence peak position could be tuned by changing the radius of the central ions of the octahedra. The comprehensive study of the structural factors and luminescence properties of this $Rb_8CuB(III)_3Cl_{18}$ structure will guide the future exploration of new metal halides for various light-emitting applications.

Conflicts of interest

The authors declare no conflicts of interest.

Acknowledgements

This work was supported by the National Natural Science Foundation of China (Grant No. 12174246 and 61875119) and Science and Technology Commission of Shanghai Municipality (Grant No. 21010501300). The authors thank BL17B1 beamline of National Facility for Protein Science in Shanghai (NFPS) at Shanghai Synchrotron Radiation Facility and 2D-SMC (proposal No. 2020-1st-2D-024) of the Pohang Accelerator Laboratory for providing the beam time.

References

1 D. Han, M. Imran, M. Zhang, S. Chang, X.-G. Wu, X. Zhang, J. Tang, M. Wang, S. Ali, X. Li, *et al.*, Efficient light-emitting diodes based on in situ fabricated FAPbBr3 nanocrystals: the enhancing role of the ligand-assisted reprecipitation process, *ACS Nano*, 2018, **12**(8), 8808–8816.
2 H. Huang, M. I. Bodnarchuk, S. V. Kershaw, M. V. Kovalenko and A. L. Rogach, Lead halide perovskite nanocrystals in the research spotlight: stability and defect tolerance, *ACS Energy Lett.*, 2017, **2**(9), 2071–2083.
3 L. Chouhan, S. Ghimire, C. Subrahmanyam, T. Miyasaka and V. Biju, Synthesis, optoelectronic properties and applications of halide perovskites, *Chem. Soc. Rev.*, 2020, **49**(10), 2869–2885.
4 Z. Xiao, Z. Song and Y. Yan, From lead halide perovskites to lead-free metal halide perovskites and perovskite derivatives, *Adv. Mater.*, 2019, **31**(47), 1803792.
5 Y.-H. Lin, N. Sakai, P. Da, J. Wu, H. C. Sansom, A. J. Ramadan, S. Mahesh, J. Liu, R. D. J. Oliver, J. Lim, *et al.*, A piperidinium salt stabilizes efficient metal-halide perovskite solar cells, *Science*, 2020, **369**(6499), 96–102.
6 K. Nishimura, M. A. Kamarudin, D. Hirotani, K. Hamada, Q. Shen, S. Iikubo, T. Minemoto, K. Yoshino and S. Hayase, Lead-free tin-halide perovskite solar cells with 13% efficiency, *Nano Energy*, 2020, **74**, 104858.
7 J. Lin, M. Lai, L. Dou, C. S. Kley, H. Chen, F. Peng, J. Sun, D. Lu, S. A. Hawks, C. Xie, *et al.*, Thermochromic halide perovskite solar cells, *Nat. Mater.*, 2018, **17**(3), 261–267.
8 Z. Ni, C. Bao, Y. Liu, Q. Jiang, W.-Q. Wu, S. Chen, X. Dai, B. Chen, B. Hartweg, Z. Yu, *et al.*, Resolving spatial and energetic distributions of trap states in metal halide perovskite solar cells, *Science*, 2020, **367**(6484), 1352–1358.
9 W. Xu, Q. Hu, S. Bai, C. Bao, Y. Miao, Z. Yuan, T. Borzda, A. J. Barker, E. Tyukalova, Z. Hu, *et al.*, Rational molecular passivation for high-performance perovskite light-emitting diodes, *Nat. Photonics*, 2019, **13**(6), 418–424.
10 Q. Shan, J. Song, Y. Zou, J. Li, L. Xu, J. Xue, Y. Dong, B. Han, J. Chen and H. Zeng, High performance metal halide perovskite light-emitting diode: from material design to device optimization, *Small*, 2017, **13**(45), 1701770.
11 M. Lu, Y. Zhang, S. Wang, J. Guo, W. W. Yu and A. L. Rogach, Metal halide perovskite light-emitting devices: promising technology for next-generation displays, *Adv. Funct. Mater.*, 2019, **29**(30), 1902008.
12 Q. Ge, R. Zheng, J. Lin and H. Chen, Cs2InCl5(H_2O): A moisture-stable defective double halide perovskite analogue with broadband emission, *Mater. Lett.*, 2020, **277**, 128280.
13 L. Sun, W. Li, W. Zhu and Z. Chen, Single-crystal perovskite detectors: development and perspectives, *J. Mater. Chem. C*, 2020, **8**(34), 11664–11674.
14 W. Zhu, W. Ma, Y. Su, Z. Chen, X. Chen, Y. Ma, L. Bai, W. Xiao, T. Liu, H. Zhu, *et al.*, Low-dose real-time X-ray imaging with nontoxic double perovskite scintillators, *Light: Sci. Appl.*, 2020, **9**, 112.
15 H. P. Wang, S. Li, X. Liu, Z. Shi, X. Fang and J. H. He, Low-dimensional metal halide perovskite photodetectors, *Adv. Mater.*, 2021, **33**(7), 2003309.
16 J. Ma, L. Zhang, J. Wang, R. Zheng, X. Feng, W. Wei, W. Zou, Z. Yang, Y. Zheng and H. Chen, A novel optical sensor for Pb2+ detection based on *in situ* formation of Ruddlesden-Popper phase (C4H9NH3)2PbBr4 perovskite, *Mater. Lett.*, 2021, 131280.
17 X. Li, F. Zhang, H. He, J. J. Berry, K. Zhu and T. Xu, On-device lead sequestration for perovskite solar cells, *Nature*, 2020, **578**(7796), 555–558.
18 M. H. Kumar, S. Dharani, W. L. Leong, P. P. Boix, R. R. Prabhakar, T. Baikie, C. Shi, H. Ding, R. Ramesh, M. Asta, *et al.*, Lead-free halide perovskite solar cells with high photocurrents realized through vacancy modulation, *Adv. Mater.*, 2014, **26**(41), 7122–7127.
19 W. Ning and F. Gao, Structural and functional diversity in lead-free halide perovskite materials, *Adv. Mater.*, 2019, **31**(22), 1900326.
20 H. Chen, S. Xiang, W. Li, H. Liu, L. Zhu and S. Yang, Inorganic perovskite solar cells: a rapidly growing field, *Sol. RRL*, 2018, **2**(2), 1700188.

21 A. H. Slavney, T. Hu, A. M. Lindenberg and H. I. Karunadasa, A bismuth-halide double perovskite with long carrier recombination lifetime for photovoltaic applications, *J. Am. Chem. Soc.*, 2016, **138**(7), 2138–2141.
22 J. Lin, H. Chen, J. Kang, L. N. Quan, Z. Lin, Q. Kong, M. Lai, S. Yu, L. Wang, L.-W. Wang, *et al.*, Copper(I)-based highly emissive all-inorganic rare-earth halide clusters, *Matter*, 2019, **1**(1), 180–191.
23 J.-P. Correa-Baena, L. Nienhaus, R. C. Kurchin, S. S. Shin, S. Wieghold, N. T. Putri Hartono, M. Layurova, N. D. Klein, J. R. Poindexter, A. Polizzotti, *et al.*, A-site cation in inorganic A3Sb2I9 perovskite influences structural dimensionality, exciton binding energy, and solar cell performance, *Chem. Mater.*, 2018, **30**(11), 3734–3742.
24 Z. Xiao, W. Meng, J. Wang, D. B. Mitzi and Y. Yan, Searching for promising new perovskite-based photovoltaic absorbers: the importance of electronic dimensionality, *Mater. Horiz.*, 2017, **4**(2), 206–216.
25 C. Katan, N. Mercier and J. Even, Quantum and dielectric confinement effects in lower-dimensional hybrid perovskite semiconductors, *Chem. Rev.*, 2019, **119**(5), 3140–3192.
26 B. Traore, L. Pedesseau, L. Assam, X. Che, J.-C. Blancon, H. Tsai, W. Nie, C. C. Stoumpos, M. G. Kanatzidis, S. Tretiak, *et al.*, Composite nature of layered hybrid perovskites: assessment on quantum and dielectric confinements and band alignment, *ACS Nano*, 2018, **12**(4), 3321–3332.
27 C. Zhou, H. Lin, J. Neu, Y. Zhou, M. Chaaban, S. Lee, M. Worku, B. Chen, R. Clark, W. Cheng, *et al.*, Green emitting single-crystalline bulk assembly of metal halide clusters with near-unity photoluminescence quantum efficiency, *ACS Energy Lett.*, 2019, **4**(7), 1579–1583.
28 C. Zhou, H. Lin, Q. He, L. Xu, M. Worku, M. Chaaban, S. Lee, X. Shi, M.-H. Du and B. Ma, Low dimensional metal halide perovskites and hybrids, *Mater. Sci. Eng., R*, 2019, **137**, 38–65.
29 C. Zhang, X. Feng, Q. Song, C. Zhou, L. Peng, J. Chen, X. Liu, H. Chen, J. Lin and X. Chen, Blue-violet emission with near-unity photoluminescence quantum yield from Cu(I)-doped Rb3InCl6 single crystals, *J. Phys. Chem. Lett.*, 2021, **12**(33), 7928–7934.
30 Z. Xiao, K. Z. Du, W. Meng, D. B. Mitzi and Y. Yan, Chemical origin of the stability difference between copper(I)-and silver(I)-Based halide double perovskites, *Angew. Chem., Int. Ed.*, 2017, **56**(40), 12107–12111.
31 C. Zhang, X. Liu, J. Chen and J. Lin, Solution and solid-phase growth of bulk halide perovskite single crystals, *Chin. J. Chem.*, 2021, **39**(5), 1353–1363.
32 R. Zhang, X. Mao, D. Zheng, Y. Yang, S. Yang and K. Han, A lead-free all-inorganic metal halide with near-unity green luminescence, *Laser Photonics Rev.*, 2020, **14**(5), 2000027.
33 R. Roccanova, A. Yangui, G. Seo, T. D. Creason, Y. Wu, D. Y. Kim, M.-H. Du and B. Saparov, Bright Luminescence from Nontoxic CsCu2X3 (X = Cl, Br, I), *ACS Mater. Lett.*, 2019, **1**(4), 459–465.
34 T. D. Creason, A. Yangui, R. Roccanova, A. Strom, M. H. Du and B. Saparov, Rb2CuX3 (X = Cl, Br): 1D all-inorganic copper halides with ultrabright blue emission and up-conversion photoluminescence, *Adv. Opt. Mater.*, 2020, **8**(2), 1901338.
35 M. R. Filip and F. Giustino, The geometric blueprint of perovskites, *Proc. Natl. Acad. Sci. U. S. A.*, 2018, **115**(21), 5397–5402.
36 C. Li, X. Lu, W. Ding, L. Feng, Y. Gao and Z. Guo, Formability of ABX3 (X = F, Cl, Br, I) halide perovskites, *Acta Crystallogr., Sect. B: Struct. Sci.*, 2008, **64**(6), 702–707.
37 L. N. Quan, R. Quintero-Bermudez, O. Voznyy, G. Walters, A. Jain, J. Z. Fan, X. Zheng, Z. Yang and E. H. Sargent, Highly emissive green perovskite nanocrystals in a solid state crystalline matrix, *Adv. Mater.*, 2017, **29**(21), 1605945.
38 H. Pan, S. Wang, X. Dao and Y. Ni, Fluorescent Zn-PDC/Tb3+ coordination polymer nanostructure: A candidate for highly selective detections of cefixime antibiotic and acetone in aqueous system, *Inorg. Chem.*, 2018, **57**(3), 1417–1425.
39 V. X. Quang, P. Van Do, N. X. Ca, L. D. Thanh, V. P. Tuyen, P. M. Tan, V. X. Hoa and N. T. Hien, Role of modifier ion radius in luminescence enhancement from 5D4 level of Tb3+ ion doped alkali-alumino-telluroborate glasses, *J. Lumin.*, 2020, **221**, 117039.
40 Z. Yuan, C. Zhou, Y. Tian, Y. Shu, J. Messier, J. C. Wang, L. J. Van De Burgt, K. Kountouriotis, Y. Xin, E. Holt, *et al.*, One-dimensional organic lead halide perovskites with efficient bluish white-light emission, *Nat. Commun.*, 2017, **8**(1), 14051.
41 J. Chen, C. Zhang, X. Liu, L. Peng, J. Lin and X. Chen, Carrier dynamic process in all-inorganic halide perovskites explored by photoluminescence spectra, *Photonics Res.*, 2021, **9**(2), 151–170.
42 Y. Zhang, B. Fan, Y. Liu, H. Li, K. Deng and J. Fan, Quasi-self-trapped Frenkel-exciton near-UV luminescence with large Stokes shift in wide-bandgap Cs4PbCl6 nanocrystals, *Appl. Phys. Lett.*, 2018, **112**(18), 183101.
43 A. Miyata, A. Mitioglu, P. Plochocka, O. Portugall, J. T.-W. Wang, S. D. Stranks, H. J. Snaith and R. J. Nicholas, Direct measurement of the exciton binding energy and effective masses for charge carriers in organic–inorganic tri-halide perovskites, *Nat. Phys.*, 2015, **11**(7), 582–587.
44 A. D. Wright, C. Verdi, R. L. Milot, G. E. Eperon, M. A. Pérez-Osorio, H. J. Snaith, F. Giustino, M. B. Johnston and L. M. Herz, Electron–phonon coupling in hybrid lead halide perovskites, *Nat. Commun.*, 2016, **7**(1), 11755.
45 J. A. Steele, P. Puech, M. Keshavarz, R. Yang, S. Banerjee, E. Debroye, C. W. Kim, H. Yuan, N. H. Heo, J. Vanacken, *et al.*, Giant electron–phonon coupling and deep conduction band resonance in metal halide double perovskite, *ACS Nano*, 2018, **12**(8), 8081–8090.
46 J. Almutlaq, J. Yin, O. F. Mohammed and O. M. Bakr, The benefit and challenges of zero-dimensional perovskites, *J. Phys. Chem. Lett.*, 2018, **9**(14), 4131–4138.
47 M. I. Saidaminov, O. F. Mohammed and O. M. Bakr, Low-dimensional-networked metal halide perovskites: the next big thing, *ACS Energy Lett.*, 2017, **2**(4), 889–896.

48 S. Adjokatse, H.-H. Fang and M. A. Loi, Broadly tunable metal halide perovskites for solid-state light-emission applications, *Mater. Today*, 2017, **20**(8), 413–424.

49 P. Han, C. Luo, S. Yang, Y. Yang, W. Deng and K. Han, All-Inorganic Lead-Free 0D Perovskites by a Doping Strategy to Achieve a PLQY Boost from <2% to 90%, *Angew. Chem., Int. Ed.*, 2020, **59**(31), 12709–12713.

50 J. Huang, T. Chang, R. Zeng, J. Yan, Q. Wei, W. Zhou, S. Cao and B. Zou, Controlled Structural Transformation in Sb-Doped Indium Halides A3InCl6 and A2InCl5·H_2O Yields Reversible Green-to-Yellow Emission Switch, *Adv. Opt. Mater.*, 2021, 2002267.

51 J. Yin, H. Yang, K. Song, A. M. El-Zohry, Y. Han, O. M. Bakr, J.-L. Brédas and O. F. Mohammed, Point defects and green emission in zero-dimensional perovskites, *J. Phys. Chem. Lett.*, 2018, **9**(18), 5490–5495.

52 R. Hamze, J. L. Peltier, D. Sylvinson, M. Jung, J. Cardenas, R. Haiges, M. Soleilhavoup, R. Jazzar, P. I. Djurovich, G. Bertrand, *et al.*, Eliminating nonradiative decay in Cu(I) emitters: >99% quantum efficiency and microsecond lifetime, *Science*, 2019, **363**(6427), 601–606.

53 N. M. Khatri, M. H. Pablico-Lansigan, W. L. Boncher, J. E. Mertzman, A. C. Labatete, L. M. Grande, D. Wunder, M. J. Prushan, W. Zhang, P. S. Halasyamani, *et al.*, Luminescence and nonlinear optical properties in copper(I) halide extended networks, *Inorg. Chem.*, 2016, **55**(21), 11408–11417.

54 I. L. Malaestean, V. C. Kravtsov, J. Lipkowski, E. Cariati, S. Righetto, D. Marinotto, A. Forni and M. S. Fonari, Partial in situ reduction of copper(II) resulting in one-pot formation of 2D neutral and 3D cationic copper(I) iodide–pyrazine coordination polymers: structure and emissive properties, *Inorg. Chem.*, 2017, **56**(9), 5141–5151.